crystals

MDPI

Article

Two Modifications of Nitrilotris(methylenephenylphosphinic) Acid: A Polymeric Network with Intermolecular $(O{=}P{-}O{-}H)_3$ vs. Monomeric Molecules with Intramolecular $(O{=}P{-}O{-}H)_3$ Hydrogen Bond Cyclotrimers

Steven Knerr [1,2], Erica Brendler [2], Robert Gericke [3], Edwin Kroke [1,4] and Jörg Wagler [1,*]

[1] Institut für Anorganische Chemie, TU Bergakademie Freiberg, D-09596 Freiberg, Germany; steven.knerr@student.tu-freiberg.de (S.K.); edwin.kroke@chemie.tu-freiberg.de (E.K.)
[2] Institut für Analytische Chemie, TU Bergakademie Freiberg, D-09596 Freiberg, Germany; erica.brendler@chemie.tu-freiberg.de
[3] Institute of Resource Ecology, Helmholtz-Zentrum Dresden-Rossendorf eV, D-01328 Dresden, Germany; gericker.chemie@gmail.com
[4] Zentrum für Effiziente Hochtemperaturstoffwandlung (ZeHS), TU Bergakademie Freiberg, D-09596 Freiberg, Germany
* Correspondence: joerg.wagler@chemie.tu-freiberg.de; Tel.: +49-3731-39-4343

Abstract: Nitrilotris(methylenephenylphosphinic) acid (**$NTPAH_3$**) was silylated using hexamethyldisilazane to produce the tris(trimethylsilyl) derivative **$NTPA(SiMe_3)_3$**. From the latter, upon alcoholysis in chloroform, **$NTPAH_3$** could be recovered. Thus, a new modification of that phosphinic acid formed. Meanwhile, **$NTPAH_3$** synthesized in aqueous hydrochloric acid crystallized in the space group *P*3*c*1 with the formation of O-H···O H-bonded networks (**$NTPAH_3{}^{P}$**), in chloroform crystals in the space group *R*3*c* formed (**$NTPAH_3{}^{M}$**), the constituents of which are individual molecules with exclusively intramolecular O-H···O hydrogen bonds. Both solids, **$NTPAH_3{}^{P}$** and **$NTPAH_3{}^{M}$**, were characterized by single-crystal X-ray diffraction, multi-nuclear (^{1}H, ^{13}C, ^{31}P) solid-state NMR spectroscopy, and IR spectroscopy as well as quantum chemical calculations (both of their individual constituents as isolated molecules as well as in the periodic crystal environment). In spite of the different stabilities of their constituting molecular conformers, the different crystal packing interactions rendered the modifications of **$NTPAH_3{}^{P}$** and **$NTPAH_3{}^{M}$** similarly stable. In both solids, the protons of the acid are engaged in cyclic $(O{=}P{-}O{-}H)_3$ H-bond trimers. Thus, the trialkylamine N atom of this compound is not protonated. IR and ^{1}H NMR spectroscopy of these solids indicated stronger H-bonds in the $(O{=}P{-}O{-}H)_3$ H-bond trimers of **$NTPAH_3{}^{M}$** over those in **$NTPAH_3{}^{P}$**.

Keywords: aminomethylenephosphinic acid; DFT calculation; Hirshfeld surface; hydrogen bond; polymorphism; solid-state NMR; X-ray diffraction

check for updates

Citation: Knerr, S.; Brendler, E.; Gericke, R.; Kroke, E.; Wagler, J. Two Modifications of Nitrilotris (methylenephenylphosphinic) Acid: A Polymeric Network with Intermolecular $(O{=}P{-}O{-}H)_3$ vs. Monomeric Molecules with Intramolecular $(O{=}P{-}O{-}H)_3$ Hydrogen Bond Cyclotrimers. *Crystals* **2024**, *14*, 662. https://doi.org/10.3390/cryst14070662

Academic Editor: Gustavo Portalone

Received: 28 June 2024
Revised: 9 July 2024
Accepted: 16 July 2024
Published: 19 July 2024

Copyright: © 2024 by the authors. Licensee MDPI, Basel, Switzerland. This article is an open access article distributed under the terms and conditions of the Creative Commons Attribution (CC BY) license (https://creativecommons.org/licenses/by/4.0/).

1. Introduction

Nitrilotris(methylenephosphinic) acids are essentially related to nitrilotris(acetic) acid **I** (Figure 1), which has been shown to crystallize as a zwitterionic compound [1,2]. The protonation of the α-amine N atom by one of the acidic groups is a common feature, which is very well known from biogenic α-amino acids [3]. Upon replacing carboxylic with phosphinic (compound **II**, [4]) or phosphonic acid groups (compound **III** [5]), the slightly more acidic P-containing acid groups (for example, PhMePOOH [6] and arylphosphinic acids of the type Aryl(H)POOH [7] were shown to be more acidic than benzoic acid) serve as protonators, and this is also true for nitrilotris(methylenephosphonic) acid **IV** [8] and compound **V** [9]. In contrast to the double-zwitterionic nature of **V**, cyclohexane-1,2-diamine derivative **VI** [10] has mono-zwitterionic features. The lone pair of its second N atom is involved in an N–H···N hydrogen bond and thus less susceptible to protonation.

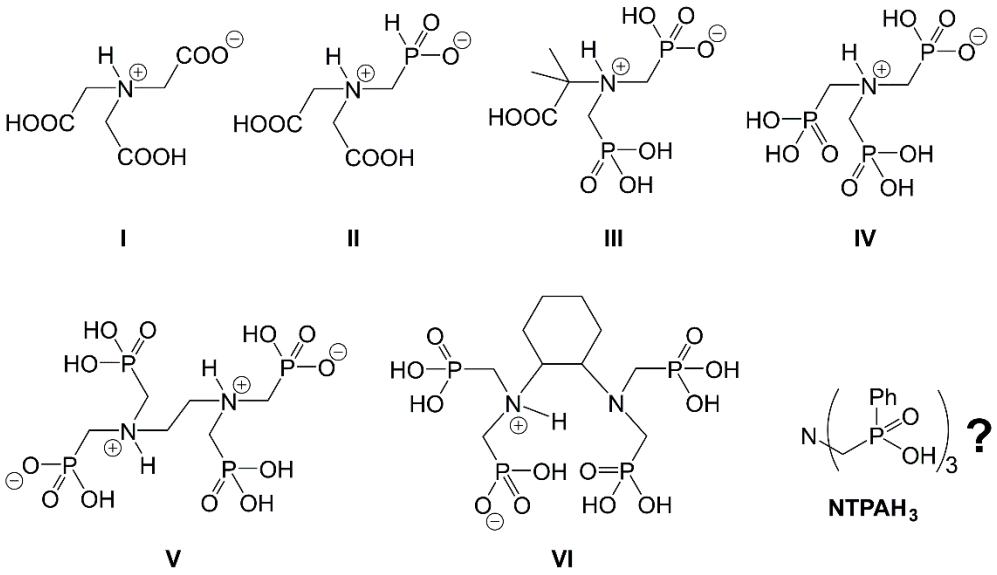

Figure 1. Selected multi-functional α-amino acids of the carboxylic, phosphinic and phosphonic acid types (**I**–**VI**) and the nitrilotris(methylenephenylphosphinic) acid (**NTPAH$_3$**) studied herein. The current study will reveal the location of the acidic protons in the latter compound.

In previous studies [11,12] nitrilotris(methylenephenylphosphinic) acid (**NTPAH$_3$**) was shown to be an interesting tripodal ligand. In the course of our ongoing investigations of Si-O-P compounds [13–15], phosphinic acids revealed interesting coordination features at silicon [16]. In this context, we prepared both **NTPAH$_3$** and its trimethylsilyl derivative **NTPA(SiMe$_3$)$_3$** as starting materials for further investigations. Thereby, we encountered highly interesting features of the molecular structure of **NTPAH$_3$** itself in the solid state, which distinguish this acid from related aminoalkyl functionalized phosphinic and phosphonic (and carboxylic) acids. Both the preference of formation of O–H···O hydrogen bonds over the protonation of the intramolecular base (i.e., the alkylamine N atom) as well as the capability of solvent-dependent formation of intramolecular vs. intermolecular $(O{=}P{-}O{-}H)_3$ H-bond trimers render crystalline **NTPAH$_3$** an interesting hydrogen bonding system. While the former stabilizes monomeric **NTPAH$_3$**, the latter renders this acid an interesting candidate as a building block for hydrogen-bonded organic frameworks (HOFs) [17–19]. As hydrogen bonding itself is of current interest (e.g., with respect to spectroscopic properties [20] and as a bond type that may complement other bond types in H-bond cross-linked materials [21]), we decided to have a closer look at this particular H-bond system of **NTPAH$_3$**.

2. Materials and Methods

2.1. General Considerations

Starting materials NH_4Cl (ORG-Laborchemie, Bunde, Germany, 99.7%), phenylphosphinic acid (Sigma-Aldrich, Steinheim, Germany, 99%), paraformaldehyde (thermo scientific, Kandel, Germany, 96%), hydrochloric acid (VWR chemicals, Fontenay-sous-bois, France, 37%), hexamethyldisilazane (abcr, Karlsruhe, Germany, 98.5%), chloroform, stabilized with amylenes (Fisher Scientific, Loughborough, UK, 99.8%), $(CD_3)_2SO$ (deutero, Kastellaun, Germany, 99.8%) and $CDCl_3$ (deutero, Kastellaun, Germany, 99.8%) were obtained from commercial suppliers. The following solvents were dried prior to use: chloroform and $(CD_3)_2SO$ were stored over 3 Å molecular sieves (Carl Roth, Karlsruhe, Germany); $CDCl_3$ was distilled from CaH_2 (Sigma-Aldrich, Steinheim, Germany, 95%) and kept under argon atmosphere.

Synthesis and characterization of **NTPA(SiMe$_3$)$_3$** were carried out under an atmosphere of dry argon utilizing standard Schlenk techniques. Solution NMR spectra (^{1}H, ^{13}C, ^{29}Si, ^{31}P) (cf. Figures S1–S7 in the supporting information) were recorded on a Nanobay

400 MHz spectrometer (Bruker Biospin, Ettlingen, Germany). ^{1}H, ^{13}C and ^{29}Si chemical shifts are reported relative to Me_4Si (0 ppm), either as internal reference or in accordance with the shift of the solvent signal ($(CD_3)_2SO$ at δ 39.5 ppm in case of the ^{13}C NMR spectrum of **NTPAH$_3$**), ^{31}P chemical shifts are reported relative to 85% H_3PO_4 (from an external calibration) set at 0 ppm. Solid-state NMR experiments (for spectra cf. Figures S8–S13 in the supporting information) were performed on an Avance HD 400 MHz WB spectrometer (Bruker Biospin, Ettlingen, Germany) with ZrO_2 rotors. The ^{13}C and ^{31}P spectra were recorded using a 4 mm triple resonance CP MAS DVT probe with a spinning rate of 10 kHz. The ^{1}H spectra were measured on a 2.5 mm CP MAS VTN probe with a spinning rate of 30 kHz. The ^{31}P NMR chemical shift was referenced to 85% H_3PO_4 using $NH_4H_2PO_4$ as external secondary standard. The ^{13}C chemical shift was referenced to TMS using adamantane as external secondary standard. Cross-polarization NMR experiments were carried out with 1 ms contact time for ^{31}P and 2 ms for ^{13}C. An 80% ramp was used for ^{31}P and a 70% ramp for ^{13}C. The recycle delay of all ^{13}C and ^{31}P CP experiments was 30 s and for ^{1}H 10 s. IR spectra were measured at room temperature using a Nicolet 380 instrument (Thermo Fisher, Waltham, MA, USA). The solid material was ground with dry KBr in a mortar and pressed into a pellet. For each measurement, 32 scans were collected using wavenumbers from 400 cm^{-1} to 4000 cm^{-1}. The spectra were corrected for background (prior to each measurement the background was collected using a freshly prepared KBr pellet).

For single-crystal X-ray diffraction analyses, crystals were selected under an inert oil and mounted on a glass capillary (which was coated with silicone grease). Diffraction data were collected on a Stoe IPDS-2/2T diffractometer (STOE, Darmstadt, Germany) using Mo Kα-radiation. Data integration was performed with the STOE software XArea version 2.3. The structures were solved using SHELXT and refined with the full-matrix least-squares methods of F^2 against all reflections with SHELXL-2019/3 [22–24]. All non-hydrogen atoms were anisotropically refined, C-bound hydrogen atoms were isotropically refined in idealized position (riding model), and hydrogen atoms of OH groups were located as residual electron density peaks and were refined without restraints. For details of data collection and refinement, see Appendix A, Table A1. Graphics of molecular structures were generated with ORTEP-3 [25,26] and POV-Ray 3.7 [27]. CCDC 2365392 (**NTPAH$_3^{P}$**), 2365391 (**NTPAH$_3^{M}$**) and 2365393 (**NTPA(SiMe$_3$)$_3$**) contain the supplementary crystal data for this article. These data can be obtained free of charge from the Cambridge Crystallographic Data Centre via https://www.ccdc.cam.ac.uk/structures/ (accessed on 25 June 2024).

The geometry optimizations of isolated molecules were carried out with ORCA 5.0.3 [28] using the restricted PBE0 functional with a relativistically recontracted Karlsruhe basis set ZORA-def2-TZVPP [29,30] for all atoms, scalar relativistic ZORA Hamiltonian [31,32], atom-pairwise dispersion correction and with the Becke–Johnson damping scheme (D3BJ) [33,34]. Calculations were started from the molecular structures obtained by single-crystal X-ray diffraction analysis. Numerical frequency calculations were performed to prove convergence at the local minimum after geometry optimization and to obtain the Gibbs free energy (293.15 K). The crystal structures of **NTPAH$_3^{P}$**, and **NTPAH$_3^{M}$** were optimized with TURBOMOLE rev. V7-7-1 [35] using the restricted PBE functional with a basis set pob-TZVP and RI-J auxiliary basis set for all atoms. A grid size of m3 and atom-pairwise dispersion correction with a Becke–Johnson damping scheme (D3BJ) [33,34] were used. During the periodic boundary optimization, the redundant coordinates were optimized and cell parameters were held constant. At the final geometry, a single-point calculation using PBE0 functional was performed. QTAIM analyses were performed with Multiwfn 3.8 [36] starting from the results obtained with the PBE0 functional. Graphics were generated using Chemcraft version 1.8 (Build 164) [37] or TURBOMOLE rev. V7-7-1 [35]. The R-factor for the match of 3-fold symmetry of the individual optimized molecular structures was evaluated with Chemcraft [37].

2.2. Syntheses and Characterization

Compound **NTPAH$_3$^{P}** ($C_{21}H_{24}NO_6P_3$). This compound was synthesized by following a published protocol [38] using NH_4Cl (1.411 g, 26.37 mmol), paraformaldehyde (4.752 g, 158.2 mmol), phenylphosphinic acid (11.24 g, 4.232 mmol), 60 mL of water and 60 mL of hydrochloric acid. Yield: 5.98 g (12.5 mmol 47%) (cf. lit. 51.5% [38]) M.p. 238 °C (cf. lit. 233-236 °C [38]). As the original report [38] did not list NMR and IR spectroscopic data, we list the data obtained from our product. **NTPAH$_3$** in solution: ^{1}H NMR (400 MHz, $(CD_3)_2SO$): δ (ppm) 13.07 (s, 3H, OH), 7.67-7.57 (m, 9H, Ph-*o*,*p*), 7.48 (m, 6H, Ph-*m*), 3.52 (d, $^{2}J_{PH}$ = 4.4 Hz, 6H, CH_2); ^{13}C NMR (101 MHz, $(CD_3)_2SO$): δ (ppm) 132.2 (Ph-*p*), 131.4 (d, $^{2}J_{PC}$ = 10.6 Hz, Ph-*o*), 130.9 (d, $^{1}J_{PC}$ = 131.5 Hz, Ph-*i*), 128.4 (d, $^{3}J_{PC}$ = 12.8 Hz, Ph-*m*), 58.9 (dt, $^{1}J_{PC}$ = 108.1 Hz, $^{3}J_{PC}$ = 5.2 Hz, CH_2); ^{31}P{^{1}H} NMR (162 MHz, $(CD_3)_2SO$): δ (ppm) 33.9. Solid **NTPAH$_3$^{P}**: IR: $\overline{\upsilon}$ (cm^{-1}) 419 (m), 476 (s), 537 (s), 694 (s), 752 (s), 763 (w), 796 (m), 886 (s), 955 (s), 987 (m), 1029 (w), 1071 (m), 1099 (m), 1099 (m), 1126 (m), 1157 (m), 1182 (s), 1246 (s), 1313 (w), 1326 (w), 1344 (m), 1394 (w), 1424 (s), 1440 (s), 1488 (w), 1592 (m), 1684 (b), 2126 (b), 2266 (b), 2560 (b), 2802 (m), 2846 (w), 2968 (m), 3056 (w).

Compound **NTPA(SiMe$_3$)$_3$** ($C_{30}H_{48}NO_6P_3Si_3$). In a 100 mL Schlenk flask with magnetic stirrer and reflux condenser, 4.793 g (10.0 mmol) of **NTPAH$_3$^{P}** were suspended in 5 mL (ca. 3.85 g, 23.9 mmol) of hexamethyldisilazane and heated with stirring. The reaction mixture was refluxed under inert atmosphere until the evolution of ammonia had ceased and a clear colorless solution was obtained. This solution was allowed to cool to room temperature within few minutes to afford a white precipitate, whereupon the supernatant was removed with a syringe and the white solid was dried in vacuo. Yield: 6.80 g (9.77 mmol, 98%).

The P atoms of this compound are centers of chirality. In $CDCl_3$ solution, this compound forms a set of diastereomeric pairs of enantiomers, the RRR/SSS pair, which was encountered in the crystal structure, and the RRS/SSR pair. We observed an RRR/SSS: RRS/SSR ratio of 85:15. Because of the chemical identity of the three phosphinic acid moieties, the former pair gives rise to a single set of signals. The latter gives rise to a double set of signals in relative 2:1 intensity ratio (these additional signals are shown in the Supplementary Material in Figures S4–S7 and listed in Table S1). RRR/SSS pair: ^{1}H NMR (400 MHz, $CDCl_3$): δ (ppm) = 7.43 (appt. tq, $^{3}J_{HH}$ = 7.5 Hz, $^{4}J_{HH}$ + $^{5}J_{PH}$ = 1.3 Hz, 3 H, Ph-*p*), 7.16 (appt. td, $^{4}J_{PH}$ = 3.6 Hz, 6 H, Ph-*m*), 7.05 (ddd, $^{3}J_{PH}$ = 12.2 Hz, $^{3}J_{HH}$ = 8.1 Hz, $^{4}J_{HH}$ = 1.4 Hz, 6 H, Ph-*o*), 4.41 (tt, $^{2}J_{HH}$ + $^{2}J_{PH}$ = 14.7, $^{4}J_{PH}$ = 2.6 Hz, 1H, CH_2), 2.60 (dd, $^{2}J_{HH}$ = 14.8, $^{2}J_{PH}$ = 11.4 Hz, 1H, CH_2), 0.17 (s, 9H, $Si(CH_3)_3$); ^{13}C{^{1}H} NMR (100 MHz, $CDCl_3$): δ (ppm) 132.0 (d, $^{2}J_{PC}$ = 10.5 Hz, Ph-*o*), 131.6 (d, $^{1}J_{PC}$ = 132.3 Hz, Ph-*i*), 131.0 (d, $^{4}J_{PC}$ = 2.8 Hz, Ph-*p*), 127.8 (d, $^{3}J_{PC}$ = 13.1 Hz, Ph-*m*), 57.2 (dt, $^{1}J_{PC}$ = 122.6 Hz, $^{3}J_{PC}$ = 9.8 Hz, CH_2), 1.27 (d, $^{3}J_{PC}$ = 1.2 Hz, $Si(CH_3)_3$); ^{29}Si{^{1}H} NMR (79 MHz, $CDCl_3$): δ (ppm) = 22.2 (d, $^{3}J_{PSi}$ = 9.3 Hz); ^{31}P{^{1}H} NMR (162 MHz, $CDCl_3$): δ (ppm) = 29.4.

A coarse crystalline product (used for single-crystal X-ray diffraction analyses) was obtained according to a related protocol but using more hexamethyldisilazane as solvent, i.e., 2.08 g (4.34 mmol) of **NTPAH$_3$^{P}** in 20 mL (ca. 15.4 g, 95.6 mmol) of hexamethyldisilazane. The greater amount of solvent caused a lower yield of isolated crystalline product (2.24 g, 3.22 mmol, 74%).

Compound **NTPAH$_3$^{M}** ($C_{21}H_{24}NO_6P_3$). In a 10 mL Schlenk flask, **NTPA(SiMe$_3$)$_3$** (0.569 g, 0.818 mmol) was dissolved in chloroform (5 mL) and anhydrous EtOH (1 mL) was added carefully (chloroform phase layered with ethanol), whereupon a small amount of white precipitate formed upon contact between the two phases within the first minute. Eventually, long crystalline needles of the product formed upon standing overnight. Thereafter, the solvent was decanted, and the white solid was dried in vacuo. Yield: 0.361 g (0.753 mmol, 92%). M.p. 238 °C. IR: $\overline{\upsilon}$ (cm^{-1}) 481 (m), 559 (s), 690(s), 712 (m), 722 (m), 734 (m), 762 (m), 957 (s), 1024 (w), 1035 (w), 1068 (w), 1097 (m), 1126 (s), 1154 (m), 1269 (w), 1310 (m), 1410 (m) 1439 (m), 1538 (b), 1595 (m), 2883 (m), 2937 (w), 2992 (w), 3051 (m).

3. Results and Discussion

3.1. Syntheses of $NTPAH_3$ and Its Trimethylsilyl Ester $NTPA(SiMe_3)_3$

The nitrilotriphosphinic acid **NTPAH$_3$** in our study was prepared according to a previously published protocol [38] (Scheme 1), and the product obtained in this procedure (referred to as modification **NTPAH$_3^P$**; the superscript index ^{P} indicates its H-bonded polymeric nature in the solid state) was used for our study. Silylation of **NTPAH$_3$** in excess hexamethyldisilazane (which served both as the silylating reagent and as the solvent) afforded the tris(trimethylsilyl) derivative **NTPA(SiMe$_3$)$_3$**, which crystallized from the reaction solution upon cooling to room temperature. This compound is highly soluble in chloroform and, in this solution, highly sensitive toward protolysis (e.g., alcoholysis). Thus, deliberate alcoholysis of **NTPA(SiMe$_3$)$_3$** in chloroform afforded long needles of **NTPAH$_3$** in a new modification (referred to as modification **NTPAH$_3^M$**, the superscript index ^{M} indicates its monomeric nature caused by exclusively intramolecular H-bonds).

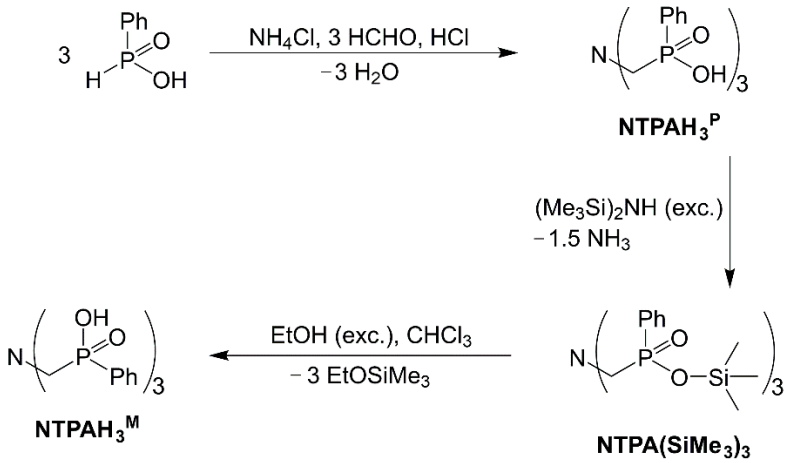

Scheme 1. Syntheses of compounds **NTPAH$_3$** (in its modifications **NTPAH$_3^P$** and **NTPAH$_3^M$**) and **NTPA(SiMe$_3$)$_3$**.

3.2. Crystallographic Analysis of the Molecular Structures of $NTPA(SiMe_3)_3$, $NTPAH_3{}^P$ and $NTPAH_3{}^M$

Compound **NTPA(SiMe$_3$)$_3$** crystallized in the trigonal space group type $R\bar{3}$ with two independent thirds of molecules in the asymmetric unit (Figure 2, Appendix A Table A1). Their N atoms are located on crystallographic 3-fold rotation axes (Figure 2b,d). The Si–O bond lengths (1.6756(14) and 1.6760(14) Å) are similar to those encountered with trimethylsilyl phosphate O=P(OSiMe$_3$)$_3$ (1.674(3) Å, [39]) and a derivative of a cyclic phosphinic acid, (Me$_3$SiO)(O=)P[-C(SiMe$_3$)$_2$–CH$_2$–CH=C(SiMe$_3$)-] (1.672(2) Å, [40]). The latter was the only hit in a CSD search [41] for crystallographically characterized triorganosilyl derivatives of phosphinic acids. Thus, the crystal structure of **NTPA(SiMe$_3$)$_3$** bears some novelty in this regard. Further metric data of these molecules (Table 1) will be discussed in the context of the further analysis of the acid **NTPAH$_3$**.

Crystals of both modifications **NTPAH$_3^P$** and **NTPAH$_3^M$** were analyzed by single-crystal X-ray diffraction (Figures 3 and 4, Tables 1 and A1). Both modifications are trigonal (space group types *P*3*c*1 and *R*3*c*, respectively), and their asymmetric units consist of one third of a molecule of **NTPAH$_3$** with its nitrogen atom located on a crystallographically imposed 3-fold rotation axis. Even though the three P-atoms within one molecule exhibit the same chirality, both crystal structures accommodate the respective (R,R,R)/(S,S,S)-pair of enantiomers because of the *c* glide in their space groups types. In both cases, the N atom is not protonated; i.e., the phosphinic acid moieties are retained. Hence, the molecules are not zwitterionic. This was an unexpected observation, as in both cases the trialkylamine N atoms' lone pairs are essentially vacant (they are not involved in any other hydrogen bonds, the structures do not contain any other H-bond donors such as

ammonium ions, water molecules etc., which could interfere with the N-located lone pair). This can be attributed to the involvement of all of the P(O)(OH) groups' hydrogen atoms in cyclic hydrogen bond patterns, i.e., $R_3^3(12)$ motifs [42] of the type $(O{=}P{-}O{-}H)_3$ (vide infra). The difference between the molecular conformations of **NTPAH$_3$** contained in its two modifications is essentially based on an approximate 110° torsion about the CH_2–P bond (N–C–P–C torsion angles are 66.7(2)° in **NTPAH$_3$^{P}** and 176.3(1)° in **NTPAH$_3$^{M}**), as shown in Figure 3. This conformational difference gives rise to entirely different inter- and intramolecular interactions. While in modification **NTPAH$_3$^{P}**, the three phenyl groups form a calix shape and the P(O)(OH) moieties point away from the central N atom (Figure 4a,c), in modification **NTPAH$_3$^{M}**, the phenyl groups represent the periphery, and the three P(O)(OH) moieties are oriented toward the central 3-fold rotation axis (Figure 4b,d). In the latter case, this orientation results in the formation of a cyclic hydrogen bond system (indicated by the thin blue lines in Figure 4d). In modification **NTPAH$_3$^{P}**, a related $R_3^3(12)$ hydrogen bond motif is formed, also about a crystallographically imposed 3-fold rotation axis, but in an intermolecular manner (cf. Figure 4e). The molecular conformation of **NTPAH$_3$** in **NTPAH$_3$^{P}** resembles the conformation of **NTPA(SiMe$_3$)$_3$**.

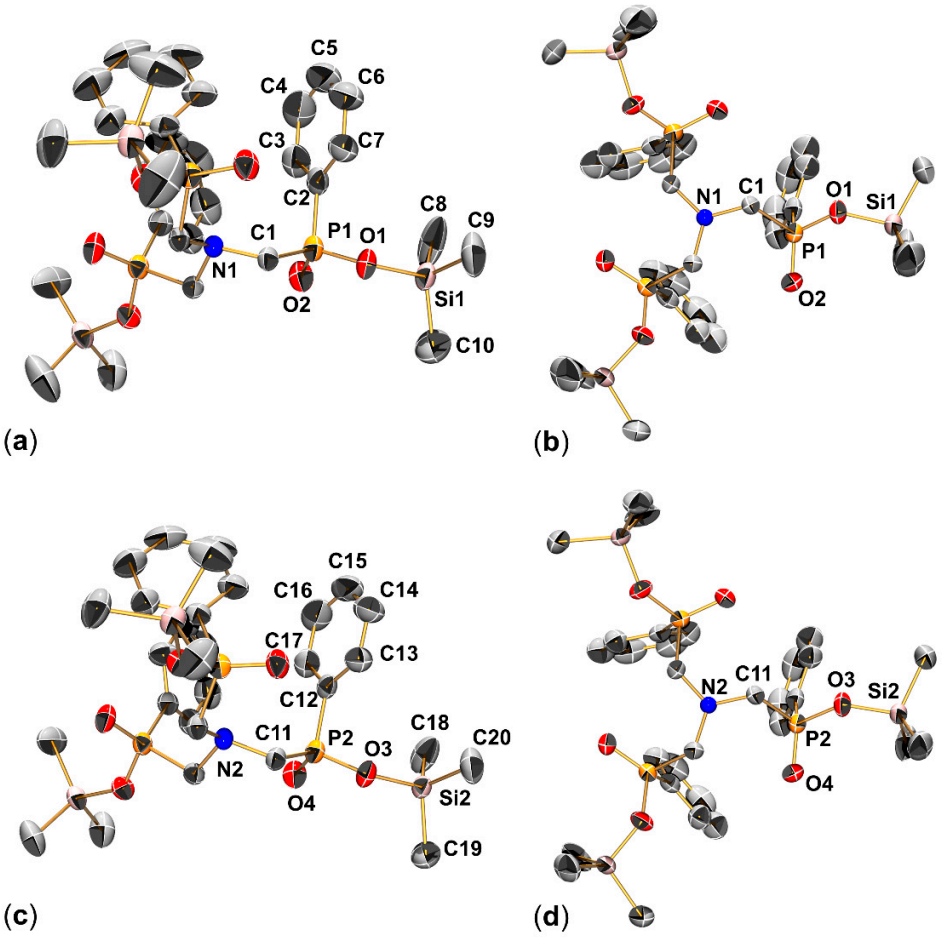

Figure 2. Molecular structure of **NTPA(SiMe$_3$)$_3$** with thermal displacement ellipsoids at the 50% probability level (for clarity, hydrogen atoms are not depicted). Sections (**a**,**c**) show a selected view of molecule 1 and 2, respectively, with the atoms of the asymmetric unit labelled, (**b**,**d**) show the molecules viewed along the crystallographic *c* axis. The two independent nitrogen atoms (N1, N2) are located on crystallographic 3-fold rotation axes; the whole molecules are generated by the symmetry operations (−x+y, −x+1, z) and (–y+1, x–y+1, z) for molecule 1, (–y+2, x–y+1, z) and (−x+y+1, −x+2, z) for molecule 2.

Table 1. Selected corresponding bond lengths (Å) and angles (deg) in the crystal structures of **NTPA(SiMe$_3$)$_3$**, **NTPAH$_3$^{P}** and **NTPAH$_3$^{M}**.

	NTPA(SiMe$_3$)$_3$ [1]	**NTPAH$_3$^{P}**	**NTPAH$_3$^{M}**
N–C	1.473(2)/1.469(2)	1.469(3)	1.467(2)
P–C(CH$_2$)	1.801(2)/1.802(2)	1.806(3)	1.817(2)
P–C(Ph)	1.788(2)/1.797(2)	1.796(3)	1.786(2)
P–O	1.575(2)/1.571(2)	1.547(2)	1.533(2)
P=O	1.469(2)/1.471(2)	1.494(2)	1.510(2)
C-N-C	110.37(12)/111.11(12)	109.56(17)	116.04(9)
N-C-P	113.21(14)/113.08(14)	115.74(18)	109.29(15)
C-P-C	107.12(10)/107.92(9)	109.81(13)	109.32(9)
O-P-O	115.57(9)/116.07(9)	115.79(15)	114.40(11)
C(CH$_2$)-P-O(H/Si)	100.15(8)/99.73(8)	98.48(13)	107.29(1)
C(CH$_2$)-P=O	114.93(9)/114.58(9)	113.47(12)	109.62(10)
C(Ph)-P-O(H/Si)	104.79(10)/104.74(9)	109.33(13)	106.67(10)
C(Ph)-P=O	112.98(11)/112.57(10)	109.46(14)	109.45(9)
Σ*X*-P=O [2]	343.5/343.2	338.7	333.5

[1] Two individual sets of parameters are given in accordance with the asymmetric unit. [2] Sum of angles about P=O (*X* = O, C).

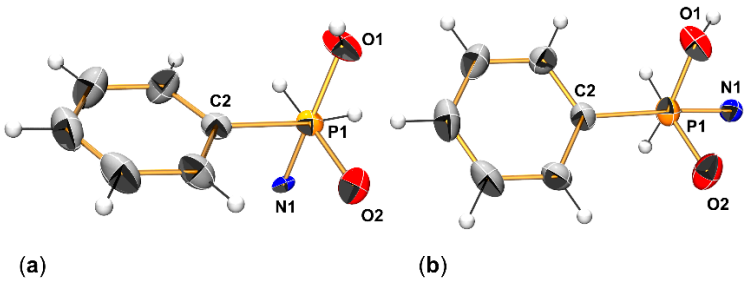

Figure 3. Thermal ellipsoid plots (50% probability) of the asymmetric units of **NTPAH$_3$** in its modifications **NTPAH$_3$^{P}** (**a**) and **NTPAH$_3$^{M}** (**b**), view along the P–CH$_2$ bond.

For a comparison of the individual molecules, a set of selected corresponding bond lengths and angles of compounds **NTPA(SiMe$_3$)$_3$**, **NTPAH$_3$^{P}** and **NTPAH$_3$^{M}** is listed in Table 1. The N-C-P angles in **NTPA(SiMe$_3$)$_3$** and **NTPAH$_3$^{P}** are noticeably wider than the tetrahedral angle, and we interpret this widening as originating from the steric congestion about the CH$_2$ groups. This angle is much closer to the tetrahedral angle in the cage structure of **NTPAH$_3$^{M}**, which lacks that kind of steric repulsion of the N- and P-bound substituents. In the compounds studied here, the coordination spheres about the P atoms are distorted tetrahedrally, which is to be expected from the VSEPR effect of the P=O bond. Thus, the widest angles are associated with *X*-P=O (*X* = C, O) moieties. Interestingly, the O-P=O angles are slightly wider than the C-P=O angles, and two reasons can be considered for this phenomenon: The C(Ph)-P=O angle is particularly small (smaller than the C(CH$_2$)-P=O angle) because of C–H···O=P attraction, which involves the P=O moiety and an ortho-H atom of the phenyl group. The C(CH$_2$)-P=O angle is still smaller than the O-P=O angle. The P–O bond may feature partial multi-bond character (in case of the P–O–Si moiety because of the electropositive silyl substituent, which renders the P–O-bound oxygen electron-rich, and in the case of the P–O–H moiety, because of the hydrogen bridge, which renders the P–O-bound oxygen electron-rich and also lowers the P=O double bond character). That would explain the enhanced O–P=O repulsion vs. relatively lowered C–P=O repulsion.

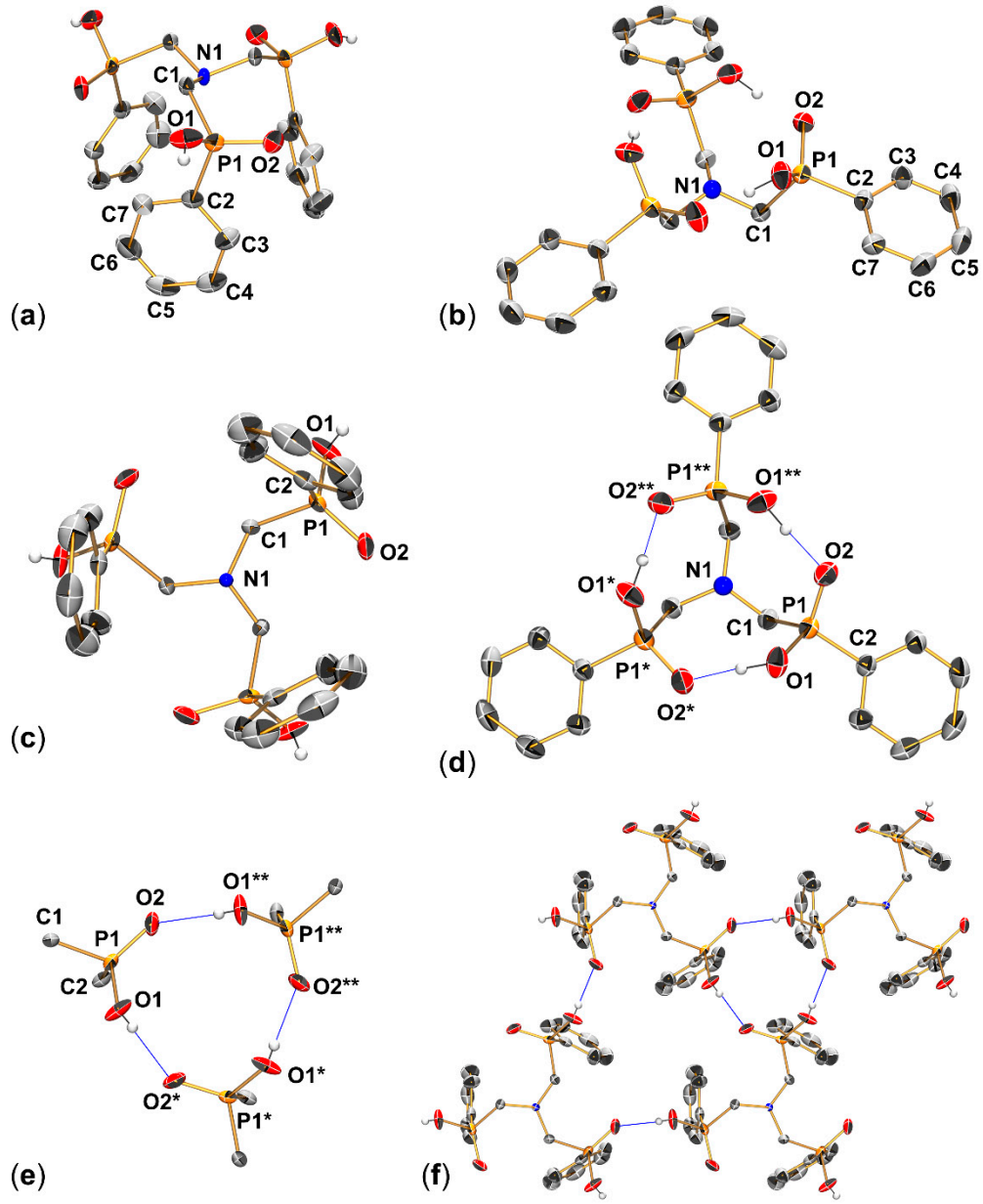

Figure 4. Molecular structures of **NTPAH$_3$** in its modifications **NTPAH$_3$^{P}** (in sections (**a**,**c**,**e**,**f**)) and **NTPAH$_3$^{M}** (in (**b**,**d**)) with thermal displacement ellipsoids at the 50% probability level (for clarity, C-bound hydrogen atoms are not depicted). Sections (**a**,**b**) show a selected view of each molecule with the atoms of the asymmetric unit labelled, (**c**,**d**) show the molecules viewed along the crystallographic *c* axis. Their nitrogen atoms (N1) are located on crystallographic 3-fold rotation axes, in both cases the whole molecules are generated by the symmetry operations (–y+1, x–y+1, z) and (−x+y, −x+1, z). For **NTPAH$_3$^{M}** these symmetry operations create a trimeric intramolecular hydrogen bond system (shown in (**d**), labels with * and ** indicate symmetry equivalents). In **NTPAH$_3$^{P}** intermolecular hydrogen bonds in a polymeric network (shown in (**f**)) give rise to a related (O=P–O–H)$_3$ motif (magnified section of interest from (**f**) shown in (**e**), these symmetry equivalents * and ** are generated by symmetry operations –y+1, x–y, z and −x+y+1, −x+1, z, respectively).

The inter- vs. intramolecular O–H···O hydrogen bonding in **NTPAH$_3$^{P}** and **NTPAH$_3$^{M}**, respectively, results in further differences between the two crystal structures: In **NTPAH$_3$^{P}** the C-N-C angles are 109.6(2)°. Thus, they are similar to the C-N-C angles in **NTPA(SiMe$_3$)$_3$** (110.4(1) and 111.1(1)°). In **NTPA$_3$^{M}**, the corresponding angles are significantly wider (116.0(1)°). We attribute this angle widening to the strain associated with the cage formation

by the intramolecular H-bonds. The metrics of the $R_3^3(12)$ motifs are different, too. With O-O-distances of 2.487(3) Å in the O–H···O motifs of **NTPAH$_3$^{P}** its intermolecular hydrogen bonds appear to be weaker than the intramolecular H-bonds in **NTPAH$_3$^{M}** with O-O-distances of 2.450(2) Å. The P=O and P–O bonds seem to exhibit notable differences, too (1.494(2) and 1.547(2) Å, respectively, in **NTPAH$_3$^{P}** vs. 1.510(2) and 1.533(2) Å, respectively, in **NTPAH$_3$^{M}**). As these features may suffer from unresolved disorder effects (simultaneous cyclic disordering of O–H···O vs. O···H–O), we employed computational analyses for closer inspection of these hydrogen bond systems (cf. Section 3.3.).

The different molecular conformations of **NTPAH$_3$** in its modifications result in different intra- and intermolecular interactions in the solid state. In particular, in **NTPAH$_3$^{M}** the O–H···O hydrogen bonds are an intramolecular feature, whereas in **NTPAH$_3$^{P}** they contribute to the intermolecular packing. To account for related kinds of interactions in a comparable manner, a Hirshfeld surface analysis was performed for the asymmetric units (which are one third molecule in each case), and therefore the O–H···O hydrogen bonds were accounted for in the same manner (Selected d_{norm} isosurface plots of the Hirshfeld surface analyses are contained in the Supplementary Material Figures S14 and S15). The d_{norm} ranges (−1.092…+2.229 for **NTPAH$_3$^{P}**, −1.094…+1.167 for **NTPAH$_3$^{M}**) vary noticeably, and the pronounced upper value of +2.229 in **NTPAH$_3$^{P}** indicates less efficient packing in this modification (well in accordance with the volume per molecule, which is much larger for **NTPAH$_3$^{P}** than for **NTPAH$_3$^{M}** with 596 vs. 549 Å^3, respectively). Figure 5 shows the fingerprint plots (d_e vs. d_i) of these analyses. Note: Because of the analysis of the asymmetric unit, the N–C bonds (and adjacent intramolecular N-H interactions) are also shown in the fingerprint plots, even though they are intramolecular features and determine the lowest d_{norm} values in both analyses. The O-H interactions are dominated by the O–H···O hydrogen bonds. Therefore, these contributions are representative of the (intermolecular and intramolecular, respectively) O–H···O hydrogen bond motifs in **NTPAH$_3$^{P}** and **NTPAH$_3$^{M}**, respectively. (C–H···O contacts are also present in both modifications; they contribute to the longer distance O-H interactions. For comparison of fingerprint plots (d_e vs. d_i) of all O-H interactions see Figure S16). Whereas these parts of the fingerprint plots are similar for the two modifications, great differences are evident for the long-range interactions part of the maps, where C-C, C-H and H-H interactions can be found, and C-C interactions are responsible for the greatest difference. Figure 6 shows that the long-range C-C interactions in **NTPAH$_3$^{P}** are caused by the calix shape created by the three phenyl groups about the 3-fold rotation axis. The faces of the phenyl rings inside the calix are thus protected from closer packing. In contrast, in **NTPAH$_3$^{M}**, the phenyl groups are more accessible for intermolecular packing from all sides. In addition to the closer C-C interactions, a larger fraction of C-C contacts on the packing of **NTPAH$_3$^{M}** results therefrom (5.8% in **NTPAH$_3$^{M}**, 2.8% in **NTPAH$_3$^{P}**) vs. a larger fraction of C-H contacts in **NTPAH$_3$^{P}** (16.8% in **NTPAH$_3$^{P}**, 12.4% in **NTPAH$_3$^{M}**), see diagram in Figure 7. In contrast, the O-H interactions (and thus the O–H···O hydrogen bonds in particular) contribute to surprisingly similar extent (26.2% in **NTPAH$_3$^{P}**, 27.8% in **NTPAH$_3$^{M}**).

Note: As the O-bound hydrogen atoms in the crystal structures of **NTPAH$_3$^{P}** and **NTPAH$_3$^{M}** were refined without restraints, the O–H bond lengths obtained from crystal structure refinement varied noticeably (0.62(4) Å in **NTPAH$_3$^{P}**, 0.93(5) Å in **NTPAH$_3$^{M}**). It is well known that there are problems associated with locating H atoms from X-ray diffraction data. In order to rule out the possibility that this deviation of different refined O–H bond lengths has greater influence on our Hirshfeld surface analysis, we performed the same analysis with structure models that were obtained by a refinement with idealized OH groups (riding model, H atom attached with the ShelX-code AFIX 147). In principle, it reflects the same findings (same appearance of fingerprint maps, same d_{norm} ranges). A representation of the contributions of contacts (corresponding to Figure 7, including the models with idealized OH groups) is included in the Supplementary Material, Figure S17.

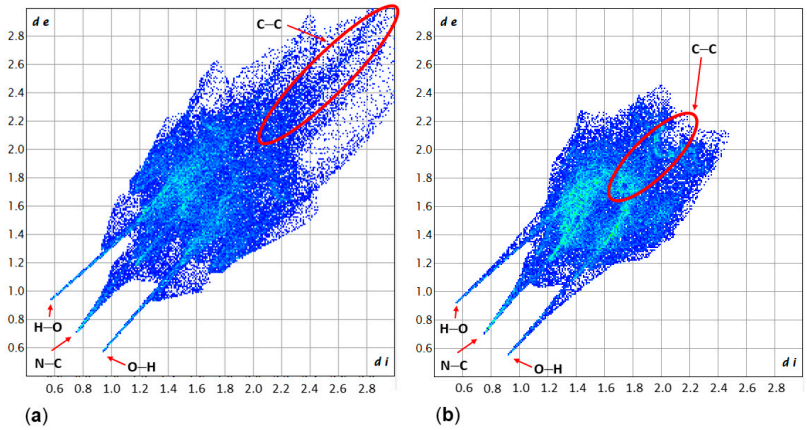

Figure 5. Fingerprint plots (d_e vs. d_i) of the Hirshfeld surface analyses (performed with CrystalExplorer version 21.5, revision 608bb32 [43]) of (**a**) the asymmetric unit of the crystal structure of **NTPAH$_3$^{P}** and (**b**) the asymmetric unit of the crystal structure of **NTPAH$_3$^{M}**. Note: The N–C interactions correspond to the N–C bonds, which connect the asymmetric unit with the two further symmetry equivalent parts of the molecule.

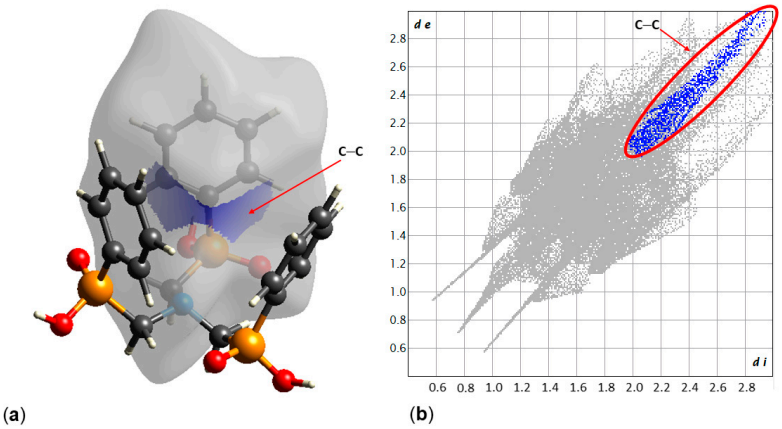

Figure 6. Selected section of the Hirshfeld surface analysis (performed with CrystalExplorer version 21.5, revision 608bb32 [43]) of the asymmetric unit of the crystal structure of **NTPAH$_3$^{P}** showing (**a**) the area of C–C interactions on the isosurface (d_{norm}) and (**b**) the corresponding section of the fingerprint plot (d_e vs. d_i).

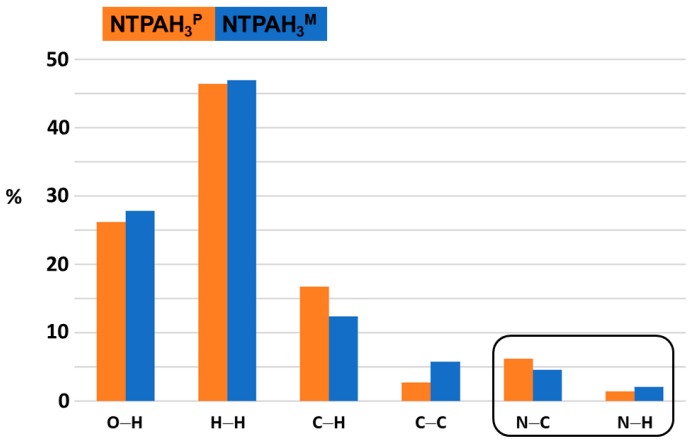

Figure 7. Percentage distribution (with respect to the area on the Hirshfeld surface) of the contacts of the asymmetric units of the crystal structures of **NTPAH$_3$^{P}** and **NTPAH$_3$^{M}**. Note: The N–C and N–H interactions (shown in the black box) correspond to the N–C bonds and interactions of N with their CH_2 H atoms. Thus, they are intramolecular interactions in both cases.

3.3. Computational Analyses of $NTPAH_3{}^P$ and $NTPAH_3{}^M$

For energetic comparison of the two modifications of **NTPAH$_3$** and for closer inspection of the H-bond situation and its influence on bond lengths, we have optimized the molecular structures of **NTPAH$_3{}^{\mathbf{P}}$** and **NTPAH$_3{}^{\mathbf{M}}$** both as isolated molecules (**NTPAH$_3{}^{\mathbf{P}}_{\mathbf{OPT\text{-}1}}$** and **NTPAH$_3{}^{\mathbf{M}}_{\mathbf{OPT\text{-}1}}$**) and in their periodic crystal environment (**NTPAH$_3{}^{\mathbf{P}}_{\mathbf{OPT\text{-}CRYST}}$** and **NTPAH$_3{}^{\mathbf{M}}_{\mathbf{OPT\text{-}CRYST}}$**). For details of the computational analyses, please see Section 2.1. and the Supplementary Material (Figures S18–S21, Tables S2–S5).

For both approaches of optimization of the molecular structures, the atomic coordinates obtained from crystallographic analyses were used as starting point, and optimizations were performed without constraints of symmetry operations. With respect to the latter, in all cases the 3-fold molecular symmetry was essentially retained in the local minima molecular conformations (with R-factors for the 3-fold symmetry match of 0.082 (**NTPAH$_3{}^{\mathbf{M}}_{\mathbf{OPT\text{-}1}}$**), 0.008 (**NTPAH$_3{}^{\mathbf{P}}_{\mathbf{OPT\text{-}1}}$**), 0.028 (**NTPAH$_3{}^{\mathbf{M}}_{\mathbf{OPT\text{-}CRYST}}$**) and 0.013 (**NTPAH$_3{}^{\mathbf{P}}_{\mathbf{OPT\text{-}CRYST}}$**), with an R-factor of 0.000 representing a perfect C_3 symmetry).

Comparison of the total energies revealed that the two modifications exhibit very similar stability with **NTPAH$_3{}^{\mathbf{M}}_{\mathbf{OPT\text{-}CRYST}}$** being only marginally less stable than **NTPAH$_3{}^{\mathbf{P}}_{\mathbf{OPT\text{-}CRYST}}$** by 0.34 kcal·mol^{-1} (PBE) or 1.66 kcal·mol^{-1} (single-point calculation with PBE0). As an isolated molecule, **NTPAH$_3{}^{\mathbf{M}}_{\mathbf{OPT\text{-}1}}$** is noticeably more stable than **NTPAH$_3{}^{\mathbf{P}}_{\mathbf{OPT\text{-}1}}$** by −20.6 kcal·mol^{-1} (PBE0). This difference is mainly attributed to the presence vs. absence of the O–H···O hydrogen bonds in **NTPAH$_3{}^{\mathbf{M}}_{\mathbf{OPT\text{-}1}}$** and **NTPAH$_3{}^{\mathbf{P}}_{\mathbf{OPT\text{-}1}}$**, respectively. Nonetheless, the energy involved in formation of the $R_3^3(12)$ H-bond trimer can be expected to exceed that value. Dimerization energies of phosphinic acids (formation of $R_2^2(8)$ motifs by two O–H···O hydrogen bonds) were experimentally determined at 21 ± 6 to 60 ± 10 kcal·mol^{-1} [44,45], which would imply H-bond energies around 10.5 to 30 kcal·mol^{-1} per H-bond and thus energies around 31.5 to 90 kcal·mol^{-1} for related H-bond cyclo-trimers. However, the energy of the molecular conformation of **NTPAH$_3{}^{\mathbf{P}}_{\mathbf{OPT\text{-}1}}$** also gains contributions from intramolecular interactions, which are associated with the formation of the (P-Ph)$_3$ calix and which are absent in **NTPAH$_3{}^{\mathbf{M}}_{\mathbf{OPT\text{-}1}}$**. These contributions serve as some compensation to the expected energy difference. Therefore, we analyzed the wave function features of the H-bonds to evaluate their energetic properties. Using quantum theory of atoms in molecules (QTAIM) analyses, we observed bond-critical points at the O–H···O hydrogen bonds. Emamian et al. [46] reported that via the electron density at the bond critical point, the hydrogen bond strength can be estimated. For **NTPAH$_3{}^{\mathbf{M}}_{\mathbf{OPT\text{-}1}}$**, an average H-bond energy of 17 kcal·mol^{-1} per H-bond is observed, and for each of the sets, **NTPAH$_3{}^{\mathbf{M}}_{\mathbf{OPT\text{-}CRYST}}$** and **NTPAH$_3{}^{\mathbf{P}}_{\mathbf{OPT\text{-}CRYST}}$**, it is ca. 20 kcal·mol^{-1}. These values are in the above-mentioned expected range of 10.5 to 30 kcal·mol^{-1} per H-bond. The energetic difference between the H-bonds of 0.4 kcal·mol^{-1} (20.3 kcal·mol^{-1} for **NTPAH$_3{}^{\mathbf{M}}_{\mathbf{OPT\text{-}CRYST}}$** and 19.9 kcal·mol^{-1} for **NTPAH$_3{}^{\mathbf{P}}_{\mathbf{OPT\text{-}CRYST}}$**) vaguely indicates stronger H-bonds in **NTPAH$_3{}^{\mathbf{M}}$** but is too marginal for a reliable conclusion.

Closer inspection of the bonds involved in the H-bond systems in **NTPAH$_3{}^{\mathbf{P}}$** and **NTPAH$_3{}^{\mathbf{M}}$** (Table 2) indicates differences between the strength of the $R_3^3(12)$ H-bond trimers in these two modifications. While in the silyl derivative **NTPA(SiMe$_3$)$_3$** the P–O bond is ca. 0.10 Å longer than the P=O bond, this bond length difference is less pronounced in the crystal structures of the acids **NTPAH$_3{}^{\mathbf{P}}$** and **NTPAH$_3{}^{\mathbf{M}}$** (with differences of 0.05 and 0.02 Å, respectively). The enhanced averaging of P–O and P=O bond lengths in **NTPAH$_3{}^{\mathbf{M}}$** could be an indication of a stronger H-bond system with respect to **NTPAH$_3{}^{\mathbf{P}}$**, and the shorter O···O distance (by 0.04 Å) in **NTPAH$_3{}^{\mathbf{M}}$** provides further support. These observations may (at least in part) also originate from unresolved O–H···O vs. O···H–O disorder in the crystal structures, and therefore further support is essential to confirm this hypothesis. Comparison of **NTPAH$_3{}^{\mathbf{P}}_{\mathbf{OPT\text{-}1}}$** (single molecule devoid of H-bonds) and **NTPAH$_3{}^{\mathbf{M}}_{\mathbf{OPT\text{-}1}}$** (single molecule with intramolecular H-bond system) already shows that P=O and P–O bonds are elongated and shortened, respectively, upon H-bond formation, and elongation of the O–H bond is observed as well. However, the additional interactions in the crystal packing cause further changes, which is evident from the comparison of **NTPAH$_3{}^{\mathbf{M}}_{\mathbf{OPT\text{-}1}}$**

and **NTPAH$_3^{M}_{OPT-CRYST}$**. Longer P=O and P–O bonds (with respect to the related bonds in the isolated molecule) are observed, and features of stronger H-bond systems are revealed. In **NTPAH$_3^{M}_{OPT-CRYST}$**, a longer O–H bond, shorter H···O distance and an overall shorter O···O distance is observed. Comparison of the two optimized molecular structures in the crystal environment (**NTPAH$_3^{P}_{OPT-CRYST}$** and **NTPAH$_3^{M}_{OPT-CRYST}$**) reveals that these modifications exhibit very similar H-bond features. Whereas in **NTPAH$_3$^{M}** the slightly longer O–H bond may indicate a stronger H-bond system, the slightly longer O···O distance is indicative of the opposite. Hence, the structural differences are less pronounced than expected from the crystallographic analysis. Therefore, further support will be delivered by solid-state ^{1}H NMR and IR spectroscopy (cf. Section 3.4). Last but not least, the different C-N-C bond angles in **NTPAH$_3$^{P}** and **NTPAH$_3$^{M}** were also confirmed by the computational analyses. Hence, the wide C-N-C angles are a characteristic feature of the cage structure of the molecule in **NTPAH$_3$^{M}**.

Table 2. Selected interatomic distances (Å) and angles (deg) in **NTPA(SiMe$_3$)$_3$** (from XRD) as well as in **NTPAH$_3$^{P}** and **NTPAH$_3$^{M}** (data from XRD and optimized molecular structures).

Compound	P=O	P–O	O–H	H···O	O···O	C-N-C
NTPA(SiMe$_3$)$_3$ (XRD)	1.469(2)	1.574(2)	-	-	-	110.4(1)
	1.471(2)	1.571(2)	-	-	-	111.1(1)
NTPAH$_3$^{P} (XRD)	1.494(2)	1.547(2)	- [1]	- [1]	2.487(3)	109.6(2)
NTPAH$_3$^{M} (XRD)	1.510(2)	1.533(2)	- [1]	- [1]	2.450(2)	116.0(1)
NTPAH$_3^{P}_{OPT-1}$ [2]	1.476	1.608	0.96	-	-	112.5
NTPAH$_3^{M}_{OPT-1}$ [2]	1.496	1.553	1.03	1.47	2.495	116.8
NTPAH$_3^{P}_{OPT-CRYST}$ [2]	1.559	1.607	1.06	1.41	2.469	109.3
NTPAH$_3^{M}_{OPT-CRYST}$ [2]	1.558	1.610	1.07	1.41	2.480	116.9

[1] The O–H bond lengths from XRD analyses are not taken into consideration for comparison because of the inherent problem of uncertainty of determination of H-atom positions by X-ray diffraction. [2] For molecules or structures with multiple independent bonds or atom distances of the same kind, the average value is reported here.

3.4. IR and Solid-State NMR Spectroscopic Analyses of NTPAH$_3$^{P} and NTPAH$_3$^{M}

The IR spectra of **NTPAH$_3$^{P}** and **NTPAH$_3$^{M}** (Figure 8) are characteristic fingerprints, which clearly distinguish between the two modifications. The most prominent difference is associated with the OH groups of these compounds. As reported earlier [47], the vibrational modes of phosphinic acids´ OH groups in cyclic hydrogen bond situations may give rise to an "A-B-C"-pattern of broad bands of high intensity. These bands are located around 2560, 2200 and 1680 cm^{-1} for **NTPAH$_3$^{P}** and around 2630, 2190 and 1540 cm^{-1} for **NTPAH$_3$^{M}**. Notably, the "C" band is shifted to lower wavenumbers and gains in relative intensity over "A" and "B" bands for **NTPAH$_3$^{M}**. In the literature [47] it is interpreted as a sign of the increasing strength of the set of hydrogen bonds involved. Furthermore, a splitting of the "B" band is particularly obvious for **NTPAH$_3$^{P}**, and in the literature that splitting has been mentioned in the context of weaker H-bonds.

^{1}H MAS NMR spectroscopy of these solids also supports the presence of stronger H-bonds in **NTPAH$_3$^{M}**. As shown in Figure 9, the signal of the OH protons (at δ_{iso} 13.6 ppm for **NTPAH$_3$^{P}** and at δ_{iso} 16.6 ppm for **NTPAH$_3$^{M}**) is sufficiently well resolved from the shift range of the aryl protons (the broad signal in the range 4–10 ppm) and thus clearly shows that the OH signal of **NTPAH$_3$^{M}** is shifted by $\Delta\delta$ ca. +3 ppm. It is well known that ^{1}H NMR signals of protons in H-bond situations are shifted to higher frequencies and that this shift is more pronounced for nuclei in stronger H-bonds [48,49]. This has been underlined by correlations of decreasing OH groups' ^{1}H NMR shielding with shortening in O···O distances in series of carboxylic acids and phosphonic acids [48]. Moreover, this shift difference of the OH signal represents the greatest difference in the ^{1}H MAS NMR spectra of these two compounds.

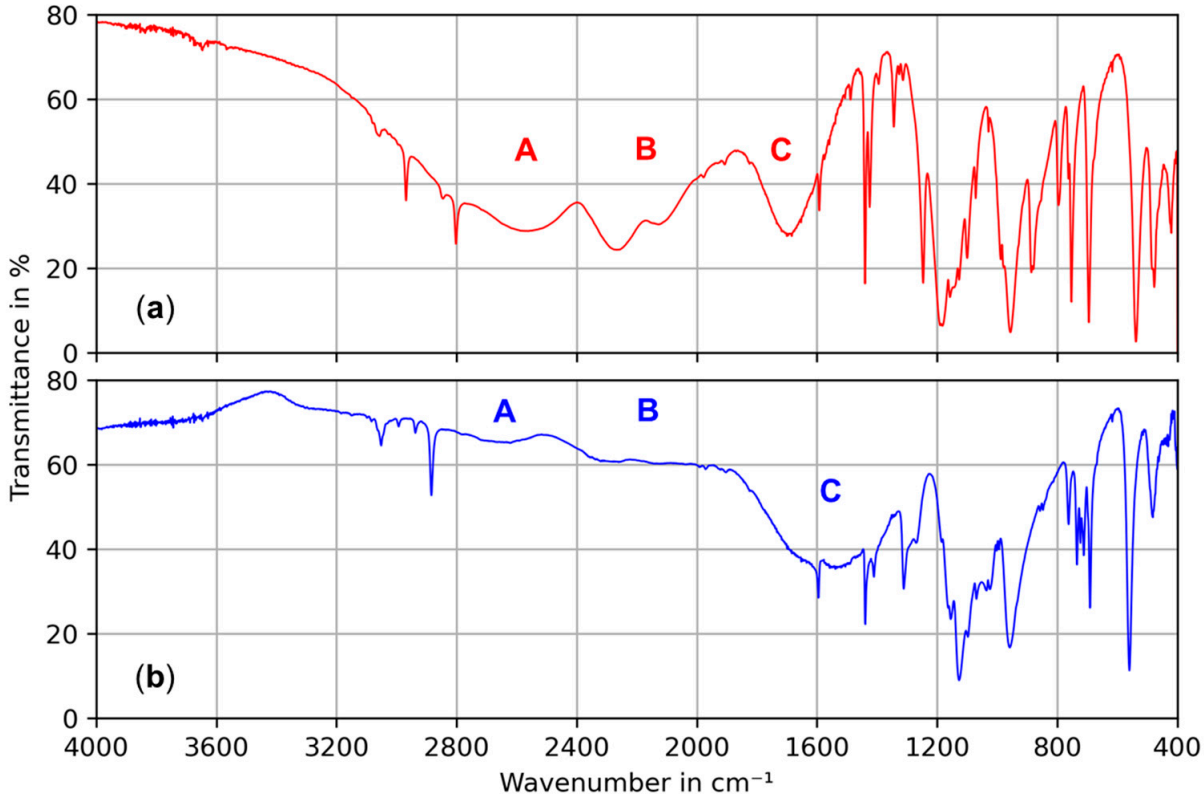

Figure 8. IR spectra of (**a**) **NTPAH$_3$^{P}** and (**b**) **NTPAH$_3$^{M}** (in KBr pellets, recorded at room temperature).

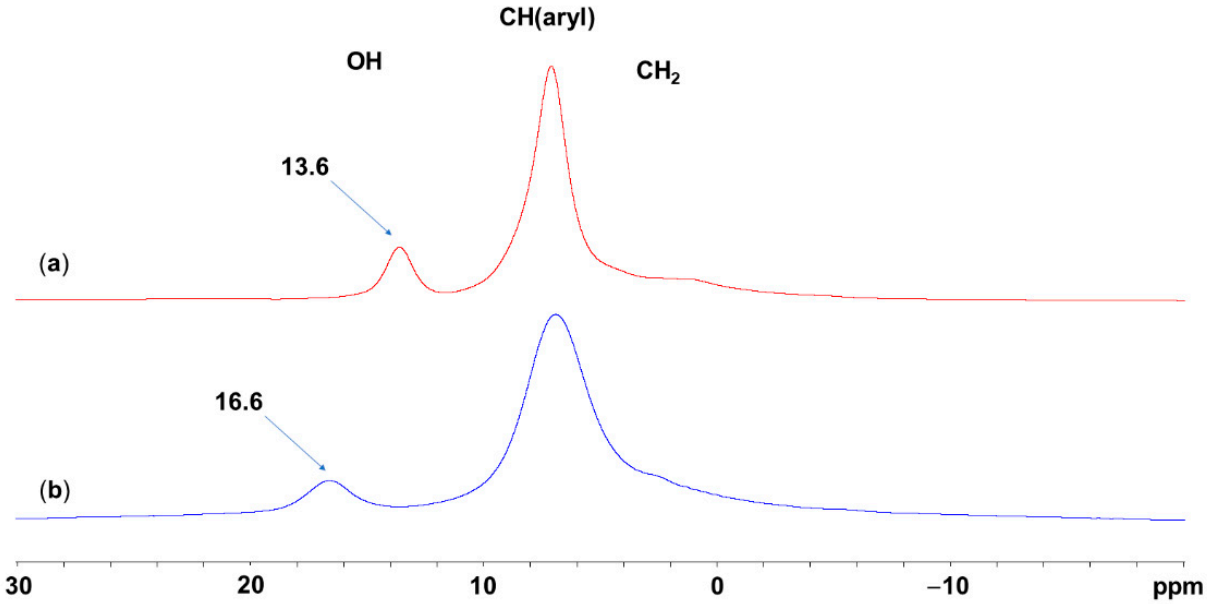

Figure 9. ^{1}H MAS NMR spectra of (**a**) **NTPAH$_3$^{P}** and (**b**) **NTPAH$_3$^{M}** recorded at MAS frequencies of 30 kHz. (The probe background has not been subtracted).

The ^{13}C MAS NMR (Figure 10) and ^{31}P MAS NMR spectra (Figure 11) reveal further spectroscopic differences between **NTPAH$_3$^{P}** and **NTPAH$_3$^{M}**. In the former, the notable shift difference $\Delta\delta$ of ca. 10 ppm between the signals of the CH_2 carbon atoms (at δ_{iso} 54 ppm for **NTPAH$_3$^{P}** and at δ_{iso} 64 ppm for **NTPAH$_3$^{M}**) indicates the involvement of these groups in different bonding situations in the two modifications (i.e., as part of a cage motif in **NTPAH$_3$^{M}** vs. absence of this motif in **NTPAH$_3$^{P}**). In contrast, the shift differences of the aromatic ^{13}C signals (in the range 125–135 ppm) are less pronounced. The ^{31}P MAS

NMR signals (at δ_{iso} 34.2 ppm for **NTPAH$_3$^{P}** and at δ_{iso} 37.7 ppm for **NTPAH$_3$^{M}**) also allow us to assign the modification to the respective solid. Both fingerprint features of the two modifications, the ^{13}C signal of the CH_2 groups and the ^{31}P signals, are sufficiently well separated to rule out the presence of significant amounts of the other modification in the respective sample.

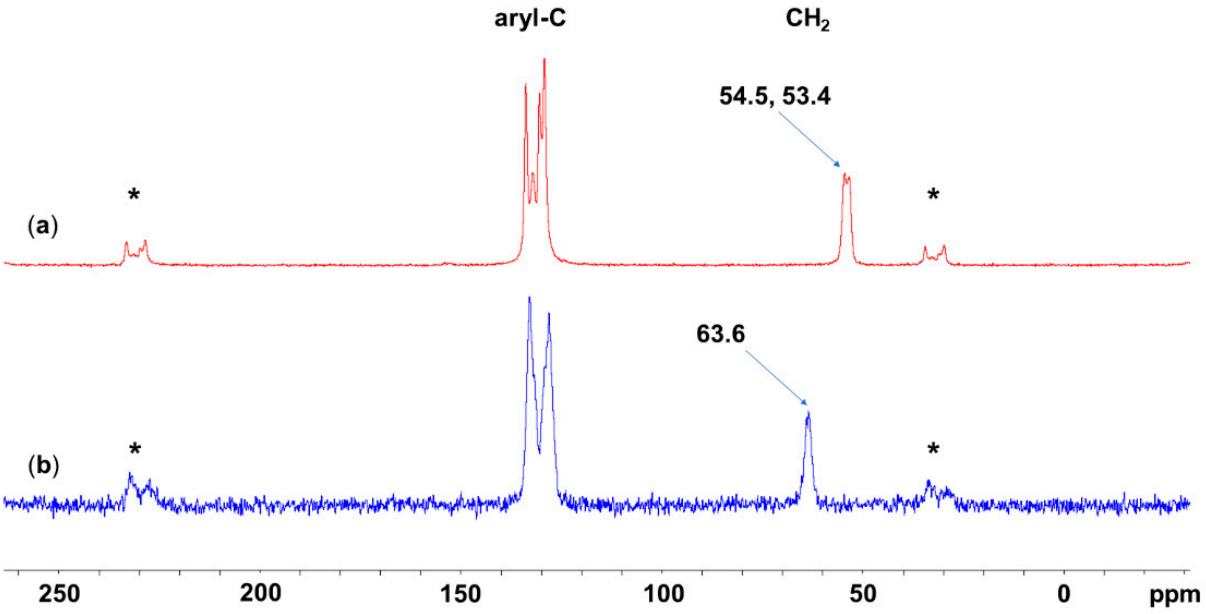

Figure 10. ^{13}C CP MAS NMR spectra of (**a**) **NTPAH$_3$^{P}** and (**b**) **NTPAH$_3$^{M}** recorded at MAS frequencies of 10 kHz. The asterisks (*) indicate spinning sidebands of the aryl-C signals.

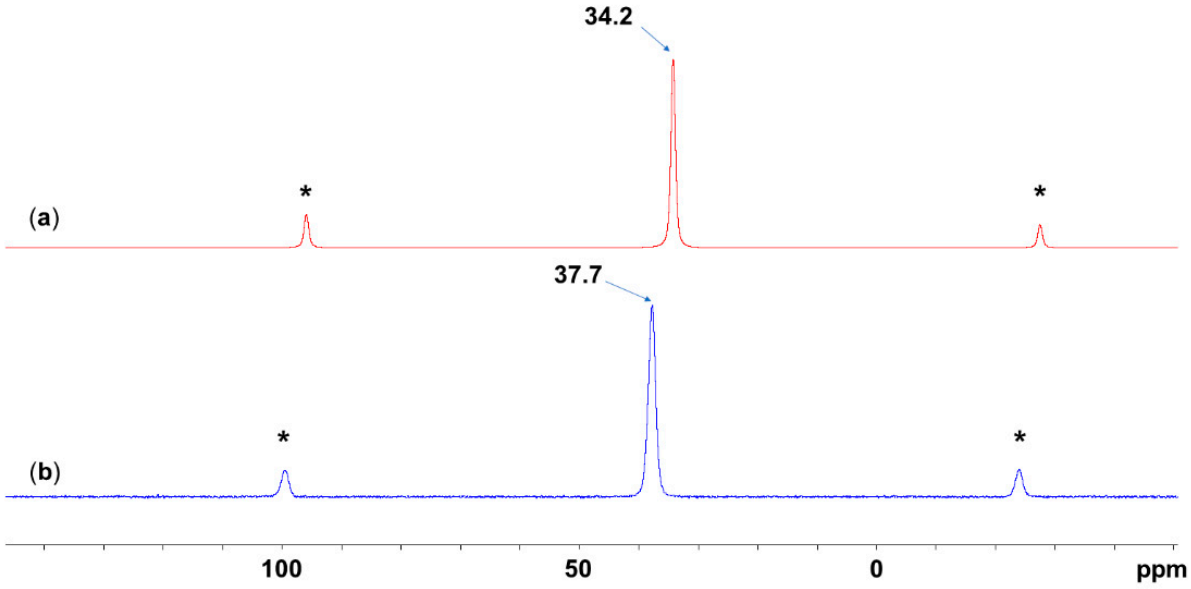

Figure 11. ^{31}P MAS NMR spectra of (**a**) **NTPAH$_3$^{P}** and (**b**) **NTPAH$_3$^{M}** recorded at MAS frequencies of 10 kHz. The asterisks (*) indicate spinning sidebands.

4. Conclusions

In general, nitrilotris(methylenephenylphosphinic) acid (**NTPAH$_3$**) can be silylated using hexamethyldisilazane to afford the tris(trimethylsilyl) derivative, **NTPA(SiMe$_3$)$_3$**. The latter is sensitive toward protolysis, and alcoholysis in chloroform liberates the acid **NTPAH$_3$**. The different solvents used for synthesis of **NTPAH$_3$** (aqueous hydrochloric acid vs. chloroform) give rise to the crystallization of two different modifications of this

acid, i.e., **NTPAH$_3$^{P}** and **NTPAH$_3$^{M}**, respectively. As both modifications exhibit similar stability (shown by computational analysis), the formation of these modifications can be attributed to the different crystallization kinetics in these different solvents, which may depend on the predominant conformer in solution. Whereas aqueous environment may foster H-bond interactions of **NTPAH$_3$** with the solvent, thus supporting the conformation encountered in **NTPAH$_3$^{P}** crystallized therefrom, chloroform cannot be involved into intermolecular H-bonds to similar extent, thus fostering the formation of intramolecular H-bonds in **NTPAH$_3$** and supporting the conformation encountered in **NTPAH$_3$^{M}** crystallized therefrom. The absence of zwitterionic species in the crystals of **NTPAH$_3$** can be attributed to the special feature of cyclic (O=P–O–H)$_3$ H-bond trimers (i.e., $R_3^3(12)$ motifs), which engage all H-bond donor and acceptor sites of the phosphinic acid moieties, thus leaving no acid for protonation of the trialkylamine N atom. Therefore, we conclude that the 3-fold symmetry of the **NTPAH$_3$** molecule, which supports crystallization in trigonal space groups and thus also supports formation of (O=P–O–H)$_3$ H-bond trimers (driven by crystal symmetry) represents a key to this rather unexpected appearance of a non-zwitterionic aminomethylphosphinic acid in its solid-state modifications. The crystal structure of **NTPA(SiMe$_3$)$_3$**, which is devoid of related H-bond systems, underlines this trend of crystallization of the **NTPA** motif in a trigonal crystal symmetry.

Molecular networks with a high density of hydrogen bonds (e.g., in layered silicon hydrogen phosphates [14] and various other H-bonded networks [50–55]) may exhibit good proton conductivity. Thus, further modification of the NTPA motif toward a covalently or coordinatively bound network with retention of O–H···O H-bond motifs and the additional trialkylamine N atoms may give rise to H^+-conductive materials. Further investigations in this direction are currently under way.

Supplementary Materials: The following supporting information can be downloaded at: https://www.mdpi.com/article/10.3390/cryst14070662/s1: NMR spectra (^{1}H, ^{13}C{^{1}H}, ^{31}P{^{1}H} and, where applicable, ^{29}Si{^{1}H}) of solutions of compounds **NTPAH$_3$** (Figures S1–S3) and **NTPA(SiMe$_3$)$_3$** (Figures S4–S7, Table S1), of solid **NTPAH$_3$^{P}** and **NTPAH$_3$^{M}** (Figures S8–S13), Hirshfeld surface analysis d_{norm} isosurface views of the asymmetric units of **NTPAH$_3$^{P}** and **NTPAH$_3$^{M}** (Figures S14 and S15), comparison of the Hirshfeld surface analysis fingerprint maps for O-H-contacts of the asymmetric units of **NTPAH$_3$^{P}** and **NTPAH$_3$^{M}** (Figure S16), comparison of the dependence of percentage of interatomic contacts on the refinement model: free vs. idealized H-refinement of OH groups (Figure S17), atomic coordinates, total energies and graphical representations of the optimized molecular structures of **NTPAH$_3$^{P}** and **NTPAH$_3$^{M}** as isolated molecules (Figures S18 and S19, Tables S2 and S3) and in the periodic crystal environment (Figures S20 and S21, Tables S4 and S5).

Author Contributions: Conceptualization, J.W.; funding acquisition, E.B., R.G. and E.K.; investigation, S.K., E.B., R.G. and J.W.; writing—original draft preparation, J.W.; writing—review and editing, S.K., E.B., R.G., E.K. and J.W.; visualization, S.K. and J.W.; supervision, E.B., E.K. and J.W. All authors have read and agreed to the published version of the manuscript.

Funding: This research was funded in part by the German Science Foundation (DFG) under Project 509900844 (Neue Si-O-P-N Verbindungen und Materialien: Synthesen, Strukturen und Materialeigenschaften) and by the German Federal Ministry of Environment, Nature Conservation, Nuclear Safety and Consumer Protection (BMUV) under Project 1501667 (Am-BALL).

Data Availability Statement: CCDC 2365392 (**NTPAH$_3$^{P}**), 2365391 (**NTPAH$_3$^{M}**) and 2365393 (**NTPA(SiMe$_3$)$_3$**) contain the supplementary crystal data for this article. These data can be obtained free of charge from the Cambridge Crystallographic Data Centre via https://www.ccdc.cam.ac.uk/structures/ (accessed on 25 June 2024).

Conflicts of Interest: The authors declare no conflict of interest.

Appendix A

Table A1. Crystallographic data from data collection and refinement for the nitrilotriphosphinic acid $N(CH_2P(Ph,O,OH))_3$ (**NTPAH$_3$**) in its modifications **NTPAH$_3^P$** and **NTPAH$_3^M$**, and for its tris(trimethylsilyl) ester $N(CH_2P(Ph,O,OSiMe_3))_3$ **NTPA(SiMe$_3$)$_3$**.

Parameter	NTPAH$_3^P$ [1]	NTPAH$_3^M$	NTPA(SiMe$_3$)$_3$ [2]
Formula	$C_{21}H_{24}NO_6P_3$	$C_{21}H_{24}NO_6P_3$	$C_{30}H_{48}NO_6P_3Si_3$
M_r	479.32	479.32	695.87
T(K)	180(2)	180(2)	160(2)
λ(Å)	0.71073	0.71073	0.71073
Crystal system	trigonal	trigonal	trigonal
Space group	*P*3*c*1	*R*3*c*	$R\bar{3}$
$a = b$(Å)	9.3792(3)	18.2554(5)	12.1818(3)
c(Å)	15.6549(6)	11.4177(3)	92.431(3)
V(Å^3)	1192.65(9)	3295.3(2)	11,878.8(7)
Z	2	6	12
ρ_{calc}(g·cm^{-1})	1.34	1.45	1.17
$\mu_{MoK\alpha}$ (mm^{-1})	0.3	0.3	0.3
F(000)	500	1500	4440
θ_{max}(°), R_{int}	28.0, 0.0662	28.0, 0.0350	25.0, 0.0492
Completeness	100%	100%	99.9%
Reflns collected	14,281	18,163	255,15
Reflns unique	1932	1748	4686
Restraints	1	1	0
Parameters	99	98	265
GoF	1.036	1.055	1.106
χ_{Flack}	0.05(6)	−0.01(3)	n/a
$R1$, $wR2$ [$I > 2\sigma(I)$]	0.0317, 0.0711	0.0224, 0.0602	0.0376, 0.1017
$R1$, $wR2$ (all data)	0.0425, 0.0742	0.0243, 0.0610	0.0550, 0.1066
Largest peak/hole (e·Å^{-3})	0.21, −0.21	0.21, −0.15	0.30, −0.24

[1] The batch of crystals contained long trigonal prisms as well as pseudo-hexagonal plates. The data set was collected from a prism. The plates represent the same modification, but they are twins according to the twin law (1 1 0, 0–1 0, 0 0–1). [2] The batch of crystals consisted of both thick plates and truncated bipyramids, both of which show trigonal symmetry. The data set was collected from a small cap of a truncated bipyramidal crystal. The central parts of the truncated bipyramids exhibited layering, which indicated stacking faults. Data collection from the larger trigonal plates revealed essentially the same unit cell parameters, but superstructure reflections along *l* indicated a primitive *c* axis of the same length. Those data sets allowed for structure solution in both space group types $R\bar{3}$ and *P*3, but both models refined to unsatisfactory *R*-values (above 0.20) and resulted in noticeable residual electron density peaks. We therefore interpret these crystals as two-phase twins, which result from large contributions of stacking faults along *c* and give rise to different local space group symmetries (i.e., space group types $R\bar{3}$ and *P*3). We are aware that these kinds of twins can be refined, for example it has been done for a 1:1 twin of space group types $P2_12_12_1$ and *Pmnb* [56], but such an analysis was beyond the scope of our study as crystal picking and collection of a data set in space group $R\bar{3}$ already provided satisfactory information of the molecular structure of compound **NTPA(SiMe$_3$)$_3$**.

References

1. Stanford, R.H., Jr. The Crystal Structure of Nitrilotriacetic Acid. *Acta Crystallogr.* **1967**, *23*, 825–832. [CrossRef]
2. Skrzypczak-Jankun, E.; Smith, D.A. Nitrilotriacetic Acid, $C_6H_9NO_6$. *Acta Crystallogr. C* **1994**, *50*, 1097–1099. [CrossRef]
3. Hoppe, B.; Martens, J. Aminosäuren—Bausteine des Lebens. *Chem. Unserer Zeit* **1983**, *17*, 4153. [CrossRef]
4. Urbanovský, P.; Kotek, J.; C´ísařová, I.; Hermann, P. Selective and clean synthesis of aminoalkyl-*H*-phosphinic acids from hypophosphorous acid by phospha-Mannich reaction. *RSC Adv.* **2020**, *10*, 21329–21349. [CrossRef] [PubMed]
5. Kasser, J.; Nazarov, A.A.; Hartinger, C.G.; Wdziekonski, B.; Dani, C.; Kuznetsov, M.L.; Arion, V.B.; Keppler, B.K. A one step/one pot synthesis of *N*,*N*-bis(phosphonomethyl)amino acids and their effects on adipogenic and osteogenic differentiation of human mesenchymal stem cells. *Bioorg. Med. Chem.* **2009**, *17*, 3388–3393. [CrossRef] [PubMed]
6. Baldwin, R.A.; Cheng, M.T. Organometalloid azides. IV. Preparation and reactions of N,N′-[p-arylenebis(diphenylphosphoranylidyne)] bis(P-phenyl phosphonamidic azides. *J. Org. Chem.* **1967**, *32*, 2636–2639. [CrossRef]
7. Quin, L.D.; Dysart, M.R. Arylphosphinic Acids: Dissociation Constants and Reaction with Diazomethane. *J. Org. Chem.* **1962**, *27*, 1012–1014. [CrossRef]
8. Daly, J.J.; Wheatley, P.J. The Crystal and Molecular Structure of Nitrilotrimethylene Triphosphonic Acid. *J. Chem. Soc. A* **1967**, *1967*, 212–221. [CrossRef]

9. Moschona, A.; Plesu, N.; Mezei, G.; Thomas, A.G.; Demadis, K.D. Corrosion protection of carbon steel by tetraphosphonates of systematically different molecular size. *Corros. Sci.* **2018**, *145*, 135–150. [CrossRef]
10. Bailly, T.; Burgada, R.; Lecouvey, M.; Neuman, A.; Prangé, T. *Trans* 1,2 diaminocyclohexane as a template in the synthesis of ligands for transition metal and actinide in vivo detoxification. *ARKIVOC* **2003**, *9*, 140–149. [CrossRef]
11. Cecconi, F.; Ghilardi, C.A.; Gili, P.; Midollini, S.; Lorenzo Luis, P.A.; Lozano-Gorrìn, A.D.; Orlandini, A. Complexation of nickel(II) and lead(II) cations with the tripodal nitrilo-tris(methylenephenylphosphinic) acid (H_3L). X-ray crystal structure of the dimer $[Ni(HL)(DMSO)]_2{\cdot}2DMSO$. *Inorg. Chim. Acta* **2001**, *319*, 67–74. [CrossRef]
12. Cecconi, F.; Ghilardi, C.A.; Lorenzo Luis, P.A.; Midollini, S.; Orlandini, A.; Dakternieks, D.; Duthie, A.; Dominguez, S.; Berti, E.; Vacca, A. Complexes of the tripodal nitrilotrimethylenetrisphosphonic (H_6L) and *P*,*P*′,*P*″-triphenylnitrilotrimethylenetrisphosphinic (H_3L°) acids with the copper(II) ion. Synthesis and characterization of $[Hpy][Cu(H_3L)(H_2O)]$ and $[Cu(HL^\circ)(py)]_2{\cdot}2Me_2CO$. *J. Chem. Soc. Dalton Trans.* **2001**, *30*, 211–217. [CrossRef]
13. Jähnigen, S.; Brendler, E.; Böhme, U.; Kroke, E. Synthesis of silicophosphates containing SiO_6-octahedra under ambient conditions—Reactions of anhydrous H_3PO_4 with alkoxysilanes. *Chem. Commun.* **2012**, *48*, 7675–7677. [CrossRef]
14. Kowalke, J.; Arnold, C.; Ponomarev, I.; Jäger, C.; Kroll, P.; Brendler, E.; Kroke, E. Structural Insight into Layered Silicon Hydrogen Phosphates Containing $[SiO_6]$ Octahedra Prepared by Different Reaction Routes. *Eur. J. Inorg. Chem.* **2019**, *2019*, 828–836. [CrossRef]
15. Viehweger, C.; Kowalke, J.; Brendler, E.; Schwarzer, S.; Vogt, C.; Kroke, E. Five- and six-fold coordinated silicon in silicodiphosphonates: Short range order investigation by solid-state NMR spectroscopy. *New J. Chem.* **2020**, *44*, 4613–4620. [CrossRef]
16. Kowalke, J.; Wagler, J.; Viehweger, C.; Brendler, E.; Kroke, E. Ionic Dissociation of $SiCl_4$: Formation of $[SiL_6]Cl_4$ with L = Dimethylphosphinic Acid. *Chem. Eur. J.* **2020**, *26*, 8003–8006. [CrossRef] [PubMed]
17. Mohan, B.; Singh, G.; Gupta, R.K.; Sharma, P.K.; Solovev, A.A.; Pombeiro, A.J.L.; Ren, P. Hydrogen-bonded organic frameworks (HOFs): Multifunctional material on analytical monitoring. *Trends Anal. Chem.* **2024**, *170*, 117436. [CrossRef]
18. Lin, R.-B.; Chen, B. Hydrogen-bonded organic frameworks: Chemistry and functions. *Chem* **2022**, *8*, 2114–2135. [CrossRef]
19. Chen, L.; Zhang, B.; Chen, L.; Liu, H.; Hu, Y.; Qiao, S. Hydrogen-bonded organic frameworks: Design, applications, and prospects. *Mater. Adv.* **2022**, *3*, 3680–3708. [CrossRef]
20. Samuel, H.S.; Nweke-Maraizu, U.; Etim, E.E. Understanding Intermolecular and Intramolecular Hydrogen Bonds: Spectroscopic and Computational Approaches. *J. Chem. Rev.* **2023**, *5*, 439–465. [CrossRef]
21. Song, P.; Wang, H. High-Performance Polymeric Materials through Hydrogen-Bond Cross-Linking. *Adv. Mater.* **2020**, *32*, 1901244. [CrossRef] [PubMed]
22. Sheldrick, G.M. SHELXT—Integrated space-group and crystal-structure determination. *Acta Crystallogr. A* **2015**, *71*, 3–8. [CrossRef] [PubMed]
23. Sheldrick, G.M. *Program for the Refinement of Crystal Structures*; SHELXL-2019/3; University of Göttingen: Göttingen, Germany, 2019.
24. Sheldrick, G.M. A short history of SHELX. *Acta Crystallogr. A* **2008**, *64*, 112–122. [CrossRef] [PubMed]
25. Farrugia, L.J. ORTEP-3 for windows—A version of ORTEP-III with a graphical user interface (GUI). *J. Appl. Crystallogr.* **1997**, *30*, 565. [CrossRef]
26. Farrugia, L.J. WinGX and ORTEP for Windows: An update. *J. Appl. Crystallogr.* **2012**, *45*, 849–854. [CrossRef]
27. POV-RAY (Version 3.7), Trademark of Persistence of Vision Raytracer Pty. Ltd., Williamstown, Victoria (Australia). Copyright Hallam Oaks Pty. Ltd., 1994–2004. Available online: http://www.povray.org/download/ (accessed on 28 June 2021).
28. Neese, F. Software update: The ORCA program system—Version 5.0. *WIREs Comput. Mol. Sci.* **2022**, *12*, e1606. [CrossRef]
29. Weigend, F.; Ahlrichs, R. Balanced basis sets of split valence, triple zeta valence and quadruple zeta valence quality for H to Rn: Design and assessment of accuracy. *Phys. Chem. Chem. Phys.* **2005**, *7*, 3297–3305. [CrossRef] [PubMed]
30. Pantazis, D.A.; Neese, F. All-electron basis sets for heavy elements. *WIREs Comput. Mol. Sci.* **2014**, *4*, 363–374. [CrossRef]
31. van Lenthe, E.; Baerends, E.J.; Snijders, J.G. Relativistic regular two-component Hamiltonians. *J. Chem. Phys.* **1993**, *99*, 4597–4610. [CrossRef]
32. van Wüllen, C. Molecular density functional calculations in the regular relativistic approximation: Method, application to coinage metal diatomics, hydrides, fluorides and chlorides, and comparison with first-order relativistic calculations. *J. Chem. Phys.* **1998**, *109*, 392–399. [CrossRef]
33. Grimme, S.; Ehrlich, S.; Goerigk, L. Effect of the damping function in dispersion corrected density functional theory. *J. Comput. Chem.* **2011**, *32*, 1456. [CrossRef] [PubMed]
34. Grimme, S.; Antony, J.; Ehrlich, S.; Krieg, H. A consistent and accurate ab initio parametrization of density functional dispersion correction (DFT-D) for the 94 elements H-Pu. *J. Chem. Phys.* **2010**, *132*, 154104–154119. [CrossRef] [PubMed]
35. Balasubramani, S.G.; Chen, G.P.; Coriani, S.; Diedenhofen, M.; Frank, M.S.; Franzke, Y.J.; Furche, F.; Grotjahn, R.; Harding, M.E.; Hättig, C.; et al. TURBOMOLE: Modular program suite for ab initio quantum-chemical and condensed-matter simulations. *J. Chem. Phys.* **2020**, *152*, 184107. [CrossRef] [PubMed]
36. Lu, T.; Chen, F. Multiwfn: A Multifunctional Wavefunction Analyzer. *J. Comput. Chem.* **2012**, *33*, 580–592. [CrossRef] [PubMed]
37. Chemcraft, Version 1.8 (Build 164). 2016. Available online: https://www.chemcraftprog.com/ (accessed on 19 September 2015).
38. Plaza, A.I.; Grim, S.O.; Motekaitis, R.J.; Martell, A.E. ETHYLENEBIS(NITRILODIMETHYLENE)TETRAKIS(PHENYLPHOSPHINIC ACID). In *Inorganic Syntheses*; Basolo, F., Ed.; McGraw-Hill, Inc.: New York, NY, USA, 1976; Volume 16, pp. 199–202. [CrossRef]

39. Nickelsen, J.; van Gerven, D.; Wickleder, M.S. In Situ single crystal growth of tris(trimethylsilyl)phosphate, $(Me_3SiO)_3PO$. *Z. Anorg. Allg. Chem.* **2022**, *648*, e202200184. [CrossRef]
40. Ishida, S.; Hirakawa, F.; Iwamoto, T. Reactions of a Stable Phosphinyl Radical with Stable Aminoxyl Radicals. *Chem. Lett.* **2015**, *44*, 94–96. [CrossRef]
41. This Refers to a Search in the Cambridge Structure Database Using ConQuest Version 2023.3.0 (Build 392113). Available online: https://www.ccdc.cam.ac.uk/solutions/software/conquest (accessed on 10 June 2024).
42. Bernstein, J.; Davis, R.E.; Shimoni, L.; Chang, N.-L. Patterns in Hydrogen Bonding: Functionality and Graph Set Analysis in Crystals. *Angew. Chem. Int. Ed.* **1995**, *34*, 1555–1573. [CrossRef]
43. Spackman, P.R.; Turner, M.J.; McKinnon, J.J.; Wolff, S.K.; Grimwood, D.J.; Jayatilaka, D.; Spackman, M.A. CrystalExplorer: A program for Hirshfeld surface analysis, visualization and quantitative analysis of molecular crystals. *J. Appl. Cryst.* **2021**, *54*, 1006–1011. [CrossRef]
44. Asfin, R.E.; Denisov, G.S.; Poplevchenkov, D.N.; Tokhadze, K.G.; Velikanova, T.V. IR υ(OH) Band and Dimerization of Phosphorus Acids in the Gas Phase and Solid State. *Pol. J. Chem.* **2002**, *76*, 1223–1231.
45. Asfin, R.E.; Denisov, G.S.; Tokhadze, K.G. The infrared spectra and enthalpies of strongly bound dimers of phosphinic acids in the gas phase. $(CH_2Cl)_2POOH$ and $(C_6H_5)_2POOH$. *J. Mol. Struct.* **2002**, *608*, 161–168. [CrossRef]
46. Emamian, S.; Lu, T.; Kruse, H.; Emamian, H. Exploring Nature and Predicting Strength of Hydrogen Bonds: A Correlation Analysis Between Atoms-in-Molecules Descriptors, Binding Energies, and Energy Components of Symmetry-Adapted Perturbation Theory. *J. Comput. Chem.* **2019**, *40*, 2868–2881. [CrossRef] [PubMed]
47. Hadzi, D. Infrared spectra of strongly hydrogen-bonded systems. *Pure Appl. Chem.* **1965**, *11*, 435–454. [CrossRef]
48. Harris, R.K.; Jackson, P.; Merwin, L.H.; Say, B.J.; Hägele, G. Perspectives in high-resolution solid-state nuclear magnetic resonance, with emphasis on combined rotation and multiple-pulse spectroscopy. *J. Chem. Soc. Faraday Trans. 1* **1988**, *84*, 3649–3672. [CrossRef]
49. Berglund, B.; Vaughan, R.W. Correlations between proton chemical shift tensors, deuterium quadrupole couplings, and bond distances for hydrogen bonds in solids. *J. Chem. Phys.* **1980**, *73*, 2037–2043. [CrossRef]
50. Chand, S.; Elahi, S.M.; Pal, A.; Das, M.C. Metal–Organic Frameworks and Other Crystalline Materials for Ultrahigh Superprotonic Conductivities of 10^{-2} s cm^{-1} or Higher. *Chem. Eur. J.* **2019**, *25*, 6259–6269. [CrossRef] [PubMed]
51. Hao, B.-B.; Wang, X.-X.; Zhang, C.-X.; Wang, Q. Two Hydrogen-Bonded Organic Frameworks with Imidazole Encapsulation: Synthesis and Proton Conductivity. *Cryst. Growth. Des.* **2021**, *21*, 3908–3915. [CrossRef]
52. Li, S.; Liu, Y.; Li, L.; Liu, C.; Li, J.; Ashraf, S.; Li, P.; Wang, B. Enhanced Proton Conductivity of Imidazole-Doped Thiophene-Based Covalent Organic Frameworks via Subtle Hydrogen Bonding Modulation. *ACS Appl. Mater. Interfaces* **2020**, *12*, 22910–22916. [CrossRef] [PubMed]
53. Staiger, A.; Paren, B.A.; Zunker, R.; Hoang, S.; Häußler, M.; Winey, K.I.; Mecking, S. Anhydrous Proton Transport within Phosphonic Acid Layers in Monodisperse Telechelic Polyethylenes. *J. Am. Chem. Soc.* **2021**, *143*, 16725–16733. [CrossRef] [PubMed]
54. Wang, K.; Li, T.; Zeng, H.; Zou, G.; Zhang, Q.; Lin, Z. Ionothermal Synthesis of Open-Framework Metal Phosphates Using a Multifunctional Ionic Liquid. *Inorg. Chem.* **2018**, *57*, 8726–8729. [CrossRef]
55. Zhang, K.-M.; Lou, Y.-L.; He, F.-Y.; Duanm, H.-B.; Huang, X.-Q.; Fan, Y.; Zhao, H.-R. The water-mediated proton conductivity of a 1D open framework inorganic-organic hybrid iron phosphate and its composite membranes. *Inorg. Chem. Commun.* **2021**, *134*, 109032. [CrossRef]
56. Caldwell, L.M.; Hill, A.F.; Rae, A.D.; Willis, A.C. Alkynylselenolatoalkylidynes: $[Mo(\equiv CSeC\equiv CR)(CO)_2\{HB(pzMe_2)_3\}]$ (R = CMe_3, $SiMe_3$; $pzMe_2$ = 3,5-Dimethylpyrazol-1-yl). *Organometallics* **2008**, *27*, 341–345. [CrossRef]

Disclaimer/Publisher's Note: The statements, opinions and data contained in all publications are solely those of the individual author(s) and contributor(s) and not of MDPI and/or the editor(s). MDPI and/or the editor(s) disclaim responsibility for any injury to people or property resulting from any ideas, methods, instructions or products referred to in the content.